Two - Dimensional Local Modeling of Thermospheric Heating and Neutral Mass Density Enhancement Driven by Alfvén Waves

AUTHOR(S):

Oigawa, T.; Shinagawa, H.; Taguchi, S.

CITATION:

Oigawa, T. ...[et al]. Two - Dimensional Local Modeling of Thermospheric Heating and Neutral Mass Density Enhancement Driven by Alfvén Waves. Journal of Geophysical Research: Space Physics 2022, 127(11): e2021JA030189.

ISSUE DATE:

2022-11

URL:

http://hdl.handle.net/2433/285911

JGR Space Physics

RESEARCH ARTICLE
10.1029/2021JA030189

Key Points:

- A new calculation method of Alfvén waves presented here allows us to capture spatially variable features in the cusp
- Alfvén resonator modes generate significant neutral upwelling at ~300 km altitude, and a cell of the neutral mass density enhancement is created at ~400 km altitude
- Alfvénic Poynting flux of roughly 20 mWm^{-2} can explain the average ~30% increase in mass density fraction observed at 400 km altitude

Supporting Information:

Supporting Information may be found in the online version of this article.

Correspondence to:

T. Oigawa,
oigawa@kugi.kyoto-u.ac.jp

Citation:

Oigawa, T., Shinagawa, H., & Taguchi, S. (2022). Two-dimensional local modeling of thermospheric heating and neutral mass density enhancement driven by Alfvén waves. *Journal of Geophysical Research: Space Physics*, *127*, e2021JA030189. https://doi.org/10.1029/2021JA030189

Received 6 DEC 2021
Accepted 30 SEP 2022

Two-Dimensional Local Modeling of Thermospheric Heating and Neutral Mass Density Enhancement Driven by Alfvén Waves

T. Oigawa[1], H. Shinagawa[2], and S. Taguchi[1]

[1]Department of Geophysics, Graduate School of Science, Kyoto University, Kyoto, Japan, [2]National Institute of Information and Communications Technology, Tokyo, Japan

Abstract In the cusp region, a significantly enhanced thermospheric mass density is commonly observed around 400 km altitude. Despite a number of studies, the enhancement mechanism has not been fully characterized. In order to determine how the Joule heating and resultant mass density enhancements are generated in the *F* region of the ionosphere during a few hours after the Alfvén resonator modes are set up, we have developed a new efficient method to calculate Alfvén waves. In this method, the Fourier transform was used, and Alfvén waves were solved as frequency-domain boundary value problems. We employed a two-dimensional local model and performed five modeling runs. The result from the modeling runs shows that the Alfvén resonator modes generate significant neutral upwelling at ~300 km altitude, which creates a "cell" of the neutral mass density enhancement at altitudes centered between 350 and 400 km. This cell becomes evident roughly 1 hr after the Alfvén resonator modes are set up, and this region continues to exist stably for 2 more hours. A fractional mass density enhancement at 400 km altitude 3 hr after the Alfvén resonator modes having an Alfvénic field-aligned current of 20 μAm^{-2} at the top boundary are set up reaches ~30%, which is consistent with the result obtained from satellite observations. In terms of the Poynting flux, this corresponds to ~20 mWm^{-2}, which is also consistent with previous satellite observations.

1. Introduction

The neutral mass density near 400 km altitude in the high-latitude dayside thermosphere can be significantly enhanced (e.g., Lühr et al., 2004). This enhancement has been estimated to be 33% on average (Kervalishvili & Lühr, 2013). This value far exceeds the predictions of empirical models, such as the NRLMSISE-00 model (Picone et al., 2002), and numerous modeling studies have attempted to explain the mass density enhancements (e.g., Brinkman et al., 2016; Crowley et al., 2010; Deng et al., 2013; Hogan et al., 2020; Lotko & Zhang, 2018; Oigawa et al., 2021; Ridley et al., 2006; Wilder et al., 2012).

Earlier modeling studies among them employed global ionosphere-thermosphere models, such as Thermospher e-Ionosphere-Mesosphere-Electrodynamics General Circulation Model (TIME-GCM) (Roble & Ridley, 1994; Roble et al., 1988) or Global Ionosphere-Thermosphere Model (GITM) (Ridley et al., 2006). Those studies were successful in reproducing a reasonable amount of mass density enhancement in the presence of extremely high energy inputs.

Wilder et al. (2012), for example, used TIME-GCM to generate a density change of more than 100% for a geomagnetic storm scenario. Deng et al. (2013) used GITM to impose an intense Poynting flux of 75 mW m^{-2} and soft particle precipitation, resulting in mass density enhancements of more than 50%. The Poynting flux of 75 mW m^{-2} is very large considering the average value at the auroral zone, that is, 10–15 mW m^{-2} (Gary et al., 1995).

By employing a high-resolution dynamical model, Brinkman et al. (2016) computed neutral responses to intermediate energy inputs, that is, 12 mW m^{-2}. Brinkman et al. (2016) used the Aerospace Dynamic Model (Walterscheid & Schubert, 1990), which is a time-dependent high-resolution two-dimensional model that includes the effects of rotation, viscosity, and heat conduction. In the context of their modeling, the Poynting flux of 12 mW m^{-2} corresponds to a cusp horizontal electric field of 60 mV m^{-1}. This electric field value is consistent with the one obtained from a satellite observation of the cusp in a moderate condition (Maynard et al., 1982). The model by

Brinkman et al. (2016) produced features found in satellite measurements. However, as they explicitly stated, their model has a limitation that ion transport is not included. In other words, they used a "fixed" ionosphere.

By expanding Shinagawa and Oyama's (2006) thermospheric model, Oigawa et al. (2021) created a two-dimensional local numerical model that includes ion dynamics. When the model was used to determine cusp mass density enhancements, Oigawa et al. (2021) required a southward electric field, which can occur more frequently in the cusp than a dawn-to-dusk electric field because the interplanetary magnetic field (IMF) tends to form a spiral garden-horse configuration. Since the equatorward part of the southward electric field in the cusp, or the upward field-aligned current region in the cusp tends to accompany soft electron precipitation for IMF $B_Y < 0$ (Taguchi et al., 1993), Oigawa et al. (2021) required that the peak of electron energy flux should be located in the middle of the equatorward part of the southward electric field. Oigawa et al. (2021) demonstrated that the Joule heating rate decreased in time due to chemical reactions and neutral-ion drag force and reproduced only about one-third of the typical magnitude of the cusp mass density enhancement for the moderate static electric field, that is, 60 mV m^{-1}.

This result indicates that other energy sources need to be considered to explain the cusp mass density enhancement quantitatively. Several previous studies have shown that the "electric field variability" plays a significant role in the enhancements of the Joule heating (e.g., Deng et al., 2009; Matsuo & Richmond, 2008; Matsuo et al., 2003; Zhu et al., 2018). This term refers to structures that are small in both space and time. Recently, Billett et al. (2021) have investigated the relationship between the cusp mass density enhancements at around 400 km altitude and downward Poynting flux by using data with a time resolution of 2 min. They have found that those two mesoscale parameters are not correlated very well, implying that energy deposition at finer scale sizes or higher altitudes is important.

According to Lühr et al. (2004), mass density enhancements frequently accompany intense field-aligned current (FAC) fluctuations. Rother et al. (2007) demonstrated that this small-scale FAC is most commonly observed at the cusp with peak values easily exceeding 100μAm^{-2}, which are frequently interpreted as evidence of ionospheric Alfvén resonator modes. The importance of Alfvén resonator modes for the Joule heating in the *F* region of the thermosphere has been investigated by Lotko and Zhang (2018), who calculated height profiles of Joule heating rates for Alfvén wave incident from the magnetosphere at frequencies from 0.05 to 2 Hz and perpendicular wavelengths at 400 km altitude from 0.5 to 20 km by using the one-dimensional electromagnetic analysis in two-dimensional geometry. Their findings indicate that superposed Alfvén wave electric fields from these frequencies and wavelengths primarily heat the *F* region and that the *F* region Joule heating rate for Alfvén variability is compared to that of quasistatic variability of comparable amplitude in the *F* region (at 400 km altitude).

Recently, Hogan et al. (2020) adapted the Alfvén wave model of Lotko and Zhang (2018) as a parameterized model in the National Center for Atmospheric Research Coupled Magnetosphere-Ionosphere-Thermosphere (NCAR CMIT) model and computed the neutral mass density response to an interplanetary stream interaction region (SIR) that swept past Earth on 26–27 March 2003. The Alfvén wave heating increases neutral mass density in the model by 20%–30% near the cusp at ∼400 km altitude during the SIR event, according to their calculations.

Although the calculated enhancement of the neutral mass density is consistent with the satellite observational enhancement, that is, ∼33% (Kervalishvili & Lühr, 2013), the treatment of the Alfvén waves in the calculation was based on a simple assumption, that is, being constant in 24 hr. We still do not understand how the Alfvén resonator modes heat the neutral atmosphere and control neutral mass density for a few hours after the Alfvén resonator modes are set up in the cusp region. We must also comprehend the behavior of the neutral mass density anomaly in the average condition, which is not related with an SIR.

The purpose of the present study is to determine how the Joule heating and resultant mass density enhancements are generated in the *F* region of the ionosphere during a few hours after the Alfvén resonator modes are set up. To that end, we devise a new method for solving Alfvén waves as frequency-domain boundary value problems rather than time-domain schemes like the finite-difference time-domain (FDTD). In previous studies, the latter technique was implemented (Hogan et al., 2020; Lotko & Zhang, 2018). By solving a system of linear equations only once, we can obtain the altitude profile of electric fields, magnetic fields, and FACs for each frequency and wavelength using the new method.

2. Model Description

2.1. Neutral Dynamics

We follow our previous work (Oigawa et al., 2021) for neutral dynamics. The continuity equation of neutrals is

$$\frac{\partial n_s}{\partial t} + \nabla \cdot (n_s \mathbf{u}_n) = 0, (s = \text{neutral}), \tag{1}$$

where n_s is the number density of neutral species s, and $\mathbf{u}_n$ is the neutral flow velocity. The subscript n denotes the neutral. H, as well as N_2, O_2, NO, N, and He, are considered neutral species. The velocity and temperature of all neutral species are assumed to be identical. In Equation 1, the production and loss of neutral species due to chemical reactions are neglected since the density of neutral species is much larger than the ion density.

The neutrals' momentum equation is as follows:

$$\frac{\partial \mathbf{u}_n}{\partial t} + (\mathbf{u}_n \cdot \nabla)\,\mathbf{u}_n + 2\boldsymbol{\Omega} \times \mathbf{u}_n = -\frac{1}{\rho_n}\nabla p_n - \nu_{ni}\,(\mathbf{u}_n - \mathbf{u}_i) + \mathbf{G} + \frac{1}{\rho_n}\nabla \cdot (\eta_n \nabla \mathbf{u}_n)\,, \tag{2}$$

where $\boldsymbol{\Omega}$, ρ_n, p_n, ν_{ni}, $\mathbf{u}_i$, $\mathbf{G}$, and η_n are the angular velocity of the Earth's rotation, the neutral mass density, the total neutral pressure, the neutral-ion collision frequency, the ion flow velocity, the gravitational acceleration, and the dynamic viscosity, respectively. The subscript i denotes the ion. We also use the energy equation of neutrals in the same form as Oigawa et al. (2021), which is

$$\frac{\partial T_n}{\partial t} + \mathbf{u}_n \cdot \nabla T_n = -\frac{R_n T_n}{c_{vn}}\nabla \cdot \mathbf{u}_n + \frac{1}{\rho_n c_{vn}}\nabla \cdot (\lambda_n \nabla T_n) + \frac{Q_n}{\rho_n c_{vn}}, \tag{3}$$

where T_n, R_n, c_{vn}, and κ are the neutral temperature, neutral specific gas constant, neutral specific heat capacity at constant volume, and heat conductivity in that order. Q_n represents the heating rate per unit volume as shown in Equations 13–15.

2.2. Ion and Electron Dynamics

We include ion species N^+, He^+, and H^+ in addition to N_2^+, O^+, NO^+, and O_2^+. This is because we compute Alfvén waves up to 4,000 km altitudes (see Section 2.2), where lighter ions become essential. The continuity equation of ions is

$$\frac{\partial n_s}{\partial t} + \nabla \cdot (n_s \mathbf{u}_s) = P_s - L_s n_s, (s = \text{ion}). \tag{4}$$

where n_s and $\mathbf{u}_s$ are the number density and the flow velocity of ion species s, respectively. P_s and L_s are the production and loss rates due to ionization, recombination, and other chemical reactions (see Appendix A in detail).

Oigawa et al. (2021) solved the ion momentum equation along the geomagnetic field, assuming that the ion flow is described by quasistatic single-fluid ambipolar diffusion. This method is used by many ionosphere-thermosphere models, including TIME-GCM and GITM. However, at high altitudes, this can be difficult. In this study, we instead solve the equation time-dependently for each ion species s as follows (the geomagnetic field is assumed to be directed downward (negative z direction)):

$$\frac{\partial w_s}{\partial z} + (\mathbf{u}_s \cdot \nabla)\, w_s = -\frac{1}{\rho_s}\frac{\partial p_s}{\partial z} + \frac{eE_a}{m_s} - G - \sum_t m_s \nu_{st}(w_s - w_t)\,, (s = \text{ion}), \tag{5}$$

where w_s, ρ_s, p_s, and m_s are the upward velocity, the mass density, the pressure, and the molecular mass, for ion species s, respectively. ν_{st} is the s-t collision frequency and e is the elementary charge. E_a is the ambipolar electric field and given by

$$E_a = -\frac{1}{n_e e}\frac{\partial p_e}{\partial z}. \tag{6}$$

In Equation 5, the sum of t includes all neutrals, ions, and electrons. We notice that the equation allows each ion species to move differently. Because the behavior of ambipolar diffusion varies with ion mass, it is preferable to treat ion transport as multi-fluid when considering multiple atomic ion species. Indeed, previous modeling studies that investigate ion transport in detail have commonly used this approach (e.g., Burleigh & Zettergren, 2017; Zettergren & Semeter, 2012).

The ion speed perpendicular to the geomagnetic field is derived by the ion drift expression as follows:

$$\mathbf{u}_{i\perp} = \mathbf{u}_{n\perp} + \frac{\nu_{in}\Omega_i}{\nu_{in}^2 + \Omega_i^2}\frac{\mathbf{E}_S + \mathbf{u}_n \times \mathbf{B}_0}{B_0} + \frac{\Omega_i^2}{\nu_{in}^2 + \Omega_i^2}\frac{(\mathbf{E}_S + \mathbf{u}_n \times \mathbf{B}_0)\times \mathbf{B}_0}{B_0^2}, \tag{7}$$

where Ω_i, $\mathbf{E}_S$, and $\mathbf{B}_0$ are the ion gyrofrequency, the quasistatic (not Alfvénic) electric field, and the geomagnetic field, respectively.

We also update our model to solve the ion and electron energy equations dynamically. Assuming that ion and electron heat flow are always directed to the magnetic field, the equations are

$$\frac{\partial T_i}{\partial t} + \mathbf{u}_i \cdot \nabla T_i = -\frac{R_i T_i}{c_{vi}}\nabla \cdot \mathbf{u}_i + \frac{1}{\rho_i c_{vi}}\frac{\partial}{\partial z}\left(\lambda_i \frac{\partial T_i}{\partial z}\right) + \frac{Q_i}{\rho_i c_{vi}}, \tag{8}$$

$$\frac{\partial T_e}{\partial t} + \mathbf{u}_e \cdot \nabla T_e = -\frac{2}{3}T_e \nabla \cdot \mathbf{u}_e + \frac{2}{3n_e k_B}\left(\frac{\partial \lambda_e}{\partial z} + \frac{5k_B j_z}{2e}\right)\frac{\partial T_e}{\partial z} + \frac{2\lambda_e}{3n_e k_B}\frac{\partial^2 T_e}{\partial z^2} + \frac{2Q_e}{3n_e k_B}, \tag{9}$$

where T_i, T_e, and k_B are the ion temperature, the electron temperature, and the Boltzmann constant, respectively. Q_i and Q_e are the ion and electron heating rates, which will be described later. λ_i and λ_e are ion and electron heat conductivity. The former is given by Banks and Kockarts (1973) and the latter by Schunk and Nagy (2009). In the heat flux, we account for thermoelectric effects (Schunk & Walker, 1970). j_z is the quasistatic current density in the z direction (equals FAC), which is calculated from the current continuity as follows:

$$j_z = -e\int_0^z \nabla_\perp \cdot [n_i(\mathbf{u}_{i\perp} - \mathbf{u}_{e\perp})]\, dz'. \tag{10}$$

We do not include Alfvénic FACs here, which produce no net currents. The electron motion perpendicular to the geomagnetic field is derived similar to Equatio 7 as follows:

$$\mathbf{u}_{e\perp} = \mathbf{u}_{e\perp} - \frac{\nu_{en}|\Omega_e|}{\nu_{en}^2 + \Omega_e^2}\frac{\mathbf{E}_S + \mathbf{u}_n \times \mathbf{B}_0}{B_0} + \frac{\Omega_e^2}{\nu_{en}^2 + \Omega_e^2}\frac{(\mathbf{E}_S + \mathbf{u}_n \times \mathbf{B}_0)\times \mathbf{B}_0}{B_0^2}. \tag{11}$$

Assuming the FAC is primarily carried by electrons, the upward motion can be given by

$$w_e = -\frac{j_z}{n_e e}. \tag{12}$$

The heating terms Q_n, Q_i, and Q_e in Equations 3, 8, and 9 are consisted of frictional heating (Q_n, Q_i, Q_e), particle heating (Q_{pn}, Q_{pe}), and viscous heating (Q_{vn}) as follows:

$$\begin{cases} Q_n = Q_{ni} + Q_{ne} + Q_{pn} + Q_{vn} \\ Q_i = Q_{in} + Q_{ie} \\ Q_e = Q_{en} + Q_{ei} + Q_{pe} \end{cases}, \tag{13}$$

$$\begin{cases} Q_{ni} = \dfrac{m_n n_n \nu_{ni}}{m_i + m_n}\left[3k_B(T_i - T_n) + m_i|\mathbf{u}_n - \mathbf{u}_i|^2\right] \\ Q_{in} = \dfrac{m_i n_i \nu_{in}}{m_i + m_n}\left[3k_B(T_n - T_i) + m_n|\mathbf{u}_n - \mathbf{u}_i|^2\right] \end{cases}, \tag{14}$$

$$\begin{cases} Q_{en} = -Q_{ne} = -\dfrac{m_e n_e \nu_{en}}{m_e + m_n} 3k_B (T_e - T_n) \\ Q_{ei} = -Q_{ie} = -\dfrac{m_e n_e \nu_{ei}}{m_e + m_i} 3k_B (T_e - T_i) \end{cases}. \tag{15}$$

We use the expressions of the frictional heating that is described in Schunk and Nagy (2009). The electron particle heating Q_{pe} is given by the "new simple parameterization" used in Smithtro and Solomon (2008). For Q_{vn} and Q_{pn}, we use the same expression as those in our previous work (Oigawa et al., 2021). Furthermore, we assume that the neutrals, ions, and electrons are all in equilibrium at the start (Oigawa et al., 2021; Shinagawa & Oyama, 2006).

EUV heating and external energy flux are balanced with heat conduction cooling in this equilibrium state. The electron temperature is crucial for the estimate of the ambipolar electric field (see Equation 6). The current modeling aims to be more precise than the modeling done by Oigawa et al. (2021), in which the electron temperature was fixed as the IRI-2016 model value (Bilitza et al., 2017).

2.3. Treatment of Alfvén Waves

We use the two-fluid (ion and electron) cold magnetized plasma equations in conjunction with the Maxwell equations to describe the propagation of Alfvén waves through the ionosphere-thermosphere region (Lotko & Zhang, 2018; Lysak, 1999). Defining $Q = \nabla_\perp \cdot \mathbf{E}_\perp$, $M = (\nabla_\perp \times \mathbf{E}_\perp) \cdot \hat{\mathbf{z}}$, and $J = (\nabla_\perp \times \mathbf{B}_\perp) \cdot \hat{\mathbf{z}}$, as was done by these authors, we can write the governing equations as follows:

$$\begin{cases} \left(\dfrac{\partial}{\partial t} + \dfrac{\sigma_P}{\epsilon}\right) Q = -V^2 \dfrac{\partial J}{\partial z} \mp \dfrac{\sigma_H}{\epsilon} M \\ \left(\dfrac{\partial}{\partial t} + \dfrac{\sigma_P}{\epsilon}\right) M = -V^2 \nabla^2 B_z \pm \dfrac{\sigma_H}{\epsilon} Q \\ \dfrac{\partial J}{\partial t} = -\dfrac{\partial Q}{\partial z} + \eta_\parallel \nabla_\perp^2 J \\ \dfrac{\partial B_z}{\partial t} = -M \end{cases}, \tag{16}$$

where σ_P, σ_H, ϵ, $\eta_\parallel$, and V, are the Pedersen conductivity, Hall conductivity, dielectric constant, magnetic diffusivity, and wave speed, respectively. These parameters are given by

$$\begin{gathered} \sigma_0 = \sum_s \frac{n_s q_s^2}{m_s \nu_{sn}}, \sigma_P = \sum_s \frac{n_s q_s^2}{m_s} \frac{\nu_{sn}}{\nu_{sn}^2 + \Omega_s^2}, \sigma_H = -\sum_s \frac{n_s q_s^2}{m_s} \frac{\Omega_s}{\nu_{sn}^2 + \Omega_s^2} \\ \epsilon = \epsilon_0 \left(1 + \sum_s \frac{\omega_{ps}^2}{\nu_{sn}^2 + \Omega_s^2}\right), \omega_{ps} = \sqrt{\frac{n_s q_s^2}{\epsilon_0 m_s}}, \\ \eta_\parallel = \frac{1}{\mu_0 \sigma_0}, V = \frac{1}{\sqrt{\mu_0 \epsilon}}, \end{gathered} \tag{17}$$

where μ_0 is the vacuum permeability and ϵ_0 is the vacuum permittivity. q_s is the electric charge of s ($q_e = -e$). All ion species and electrons are denoted by the subscript s. Although the original form by Lysak (1999) includes the electron inertial effect, we, like Lotko and Zhang (2018), ignore it. Unless the wavelength perpendicular to the geomagnetic field is too small, this assumption is correct.

It is assumed that the angular wave frequency ω is much less than the ion gyrofrequency Ω_i, such as $\omega^2 \ll \Omega_i^2$ and $\omega \nu_{in} \ll \Omega_i^2$. Equation 16 describes both the (shear) Alfvén and compressional magnetosonic waves. For the sake of simplicity, we will consider the one-dimensional propagation of monochromatic waves. The wavenumber perpendicular to the geomagnetic field is $k_\perp$. In this situation, $\nabla_\perp$ can be replaced with $ik_\perp$.

The Alfvén wave variables (Q and J) in (16) decouple from the compressional wave variables (M and B_z) when

$$k_\perp^2 \gg \frac{\mu_0 \omega \sigma_H^2}{\sigma_P}, \tag{18}$$

and this condition is satisfied under reasonable assumptions as shown in Lotko and Zhang (2018). In this case, the last term of the first equation in (16) may be neglected, and the first and third equations in Equation 16 alone are sufficient to solve for Q and J. Therefore, defining $\alpha = \sigma_P/\epsilon$ and $\beta = k_\perp^2 \eta_\parallel$, the equations can be written as the telegraphic equations, such as

$$\begin{cases} \left(\frac{\partial}{\partial t} + \alpha\right) Q = -V^2 \frac{\partial J}{\partial z} \\ \left(\frac{\partial}{\partial t} + \beta\right) J = -\frac{\partial Q}{\partial z} \end{cases}. \tag{19}$$

Let x, y, and z axes be directed eastward, northward, and upward, respectively. Assuming that the electric field and magnetic field oscillate in the y direction and x direction, respectively, Q and J are given as follows:

$$\begin{cases} Q = ik_\perp E_y \\ J = -ik_\perp B_x \end{cases}. \tag{20}$$

Previously, Lotko and Zhang (2018) and Hogan et al. (2020) used the FDTD method to solve Equation 19. Instead, we apply the Fourier transform to Equation 19 to obtain the frequency-domain equations shown below, assuming that the coefficients vary much slower than electromagnetic fields

$$\begin{cases} (i\omega + \alpha)\hat{Q} = -V^2 \frac{\partial \hat{J}}{\partial z} \\ (i\omega + \beta)\hat{J} = -\frac{\partial \hat{Q}}{\partial z} \end{cases}. \tag{21}$$

The functions of time and height ($Q(t, z)$ and $J(t, z)$) now become functions of frequency and altitude ($\hat{Q}(\omega, z)$ and $\hat{J}(\omega, z)$). Eliminating $\hat{J}$, we get the closed equation of $\hat{Q}$ as follows:

$$\left[\left(\alpha\beta - \omega^2\right) + i\omega(\alpha + \beta)\right] \hat{Q} + \frac{V^2}{i\omega + \beta} \frac{\partial \beta}{\partial z} \frac{\partial \hat{Q}}{\partial z} = V^2 \frac{\partial^2 \hat{Q}}{\partial z^2}. \tag{22}$$

Then, $\hat{J}$ is given by

$$\hat{J} = -\frac{1}{i\omega + \beta} \frac{\partial \hat{Q}}{\partial z}. \tag{23}$$

We can see from Equations 19 and 21 that the time-domain initial value problem is transformed into a frequency-domain boundary value problem.

Using the concept of Mur's absorbing boundary condition, the bottom (Earth's surface) boundary condition is provided (Mur, 1981). If waves propagate to the negative z-direction without any reflection or dissipation, the time-domain equation at $z = 0$ is written as

$$\frac{\partial Q(t, 0)}{\partial t} = V(0) \frac{\partial Q(t, z)}{\partial z}\bigg|_{z=0}. \tag{24}$$

This equation is transformed into the frequency-domain as follows:

$$\frac{\partial \hat{Q}(\omega, z)}{\partial z}\bigg|_{z=0} = \frac{i\omega}{V(0)} \hat{Q}(\omega, 0). \tag{25}$$

At the top boundary (at $z = z_{\text{top}}$), we set an input value as $\hat{Q}\left(z_{\text{top}}\right) = \hat{Q}_{\text{input}}$ ($z_{top} = 4,000$km in this calculation, see Section 2.4).

Finally, Equation 22 is discretized, yielding a system of linear equations as follows:

$$\begin{bmatrix} C & -1 & & & & & \\ B_1^- & A_1 & B_1^+ & & & & \\ & B_2^- & A_2 & B_2^+ & & & \\ & & \ddots & \ddots & \ddots & & \\ & & & B_{N-2}^- & A_{N-2} & B_{N-2}^+ & \\ & & & & 0 & 1 & \end{bmatrix} \begin{bmatrix} \hat{Q}_0 \\ \hat{Q}_1 \\ \hat{Q}_2 \\ \vdots \\ \hat{Q}_{N-2} \\ \hat{Q}_{N-1} \end{bmatrix} = \begin{bmatrix} 0 \\ 0 \\ 0 \\ \vdots \\ 0 \\ \hat{Q}_{\text{input}} \end{bmatrix} \tag{26}$$

$$A_j = \frac{\Delta z^2}{V_j^2}\left[\left(\alpha_j\beta_j - \omega^2\right) + i\omega(\alpha_j + \beta_j)\right] + 2$$

$$B_j^{\pm} = \pm\frac{1}{4}\frac{\beta_{j+1} - \beta_{j-1}}{i\omega + \beta_j} - 1, C = \frac{2V_0 + i\omega\Delta z}{2V_0 - i\omega\Delta z}$$

Since the coefficient of the left-hand side is a tridiagonal matrix, the system of equations is easily solved in the calculation cost of O(N).

The benefit of this approach is that it significantly reduces calculation costs. Even for a single period, time-domain methods, such as the FDTD, require numerous iterations to reproduce Alfvén waves propagating through the ionosphere-thermosphere. In contrast, to calculate the Joule heating produced by Alfvén waves, we only need the height profile of the average amplitude of electromagnetic fields rather than the time evolution. This new method allows us to obtain the altitude profile of electric fields, magnetic fields, and FACs for each frequency and wavelength by solving a system of linear equations once. The Alfvén speed reaches the maximum $V_{\max} \sim 1.5 \times 10^7$ m s^{-1} at 3,970 km altitude. (Regions with no ions, where Alfvén speed becomes the speed of light, are excluded.) Therefore, the Courant-Friedrichs-Lewy condition requires that the time step be smaller than $\Delta z / V_{\max} \sim 3.3 \times 10^{-4}$ s when using the FDTD method ($\Delta z = 5$ km in this model). This value indicates that each grid requires 30,000 iterations to calculate a 0.1 Hz period (150,000 iterations if 0.02 Hz). Equation 26 on the other hand, can be solved with a calculation cost comparable to only "one" iteration of the FDTD method. We note, however, that it is also true that the FDTD method has the strength of being suitable for dealing with transient events that are not treatable as a time-harmonic boundary-value problem.

Rother et al. (2007) have shown that the spectral amplitude of FAC by Alfvén waves measured by the 50-Hz magnetometer on CHAMP is nearly constant against frequency. Using Swarm observations, Consolini et al. (2020) discovered that the power spectrum density (PSD) of the magnetic field fluctuation perpendicular to the geomagnetic field is inversely proportional to the square of the frequency, which is equivalent to Rother et al.'s results. The CHAMP measurements exhibit a "cut-off" frequency at ∼8 Hz, where the amplitude sharply diminishes. Rother et al. (2007) interpreted the structure of FACs as spatial variability and estimated the scale size to be ∼1 km. It would be then proper to set $\hat{Q}_{\text{input}}$ constant against the perpendicular wavelength $\lambda_\perp$ and the minimum $\lambda_\perp$ to be 1 km.

Lühr et al. (2015) defined "large-scale" as greater than 150 km and "small-scale" as less than 10 km with the latter being carried primarily by kinetic Alfvén waves. Yokoyama et al. (2020, 2021) also demonstrated that FACs with spatial scales of 20–30 km are quasistatic (not Alfvénic). Based on these results, we take $\lambda_\perp$ to be ≤20 km.

We let the maximum frequency be 2 Hz. This value is close to the proton gyrofrequency in the dayside magnetopause. Thus, Alfvén waves above this frequency are absorbed by ion cyclotron resonance and rarely propagate into the ionosphere (Hogan et al., 2020; Lotko & Zhang, 2018). In this study, we assume that $\hat{Q}_{\text{input}}$ is constant with respect to frequency as well as perpendicular wavelength. This assumption is introduced because sufficient information based on observational data has not been available to date. Note that the boundary condition is just one possibility, and we do not claim that the frequency-wavelength dependence shown in Figures 2 and 3 reflects all actual situations. However, since the height dependency obtained by integrating on all frequencies and wavelengths is more important in this study than the wave spectrum at the boundary condition, this assumption would be reasonable at this time.

We discretize the frequency range, 0.02–2.00 Hz, into f_k modes, $k = 1, 2, ..., K$ with $K = 100$ and $\Delta f_k = 0.02$ Hz and the perpendicular wavelength range, 1–20 km, into $\lambda_{\perp l}$ modes, $l = 1, 2, ..., L$ with $L = 39$ and $\Delta\lambda_{\perp l} = 0.5$ km. For the perpendicular wavelength and magnetic diffusivity, we scale in the same way as Lotko and Zhang (2018), taking into account the spatial variation of the magnetic field. The values of $\lambda_\perp$ used in this paper are those estimated at the ground ($z = 0$ km).

We give the input parameter $\hat{Q}_{\text{input}}$ assuming that every mode has the same amplitude regardless of f_k or $\lambda_{\perp l}$ as follows:

$$\hat{Q}_{\text{input}}\left(f_k, \lambda_{\perp_l}\right) = \frac{\sqrt{K}}{L}\mu_0 V\left(z_{\text{top}}\right) j_A. \tag{27}$$

j_A has a dimension of current density and represents the standard FAC at the top boundary. We can obtain $\hat{Q}$ and $\hat{J}$ for each f_k and $\lambda_{\perp l}$ by solving Equation 26, and then obtaining the PSD of E_y and B_x by Equation 20. Finally, the RMS amplitude of the electric field, magnetic field, and FAC is calculated by superposing (summing over) all modes (frequencies and wavelengths). The coefficient $\sqrt{K}/L$ in Equation 27 ensures the RMS of $\hat{Q}_{\text{input}}$ equals to $\mu_0 V\left(z_{\text{top}}\right) j_A$.

Dividing the electric field $\mathbf{E}$ into the DC (quasistatic) $\mathbf{E}_S$ and AC (Alfvénic) $\mathbf{E}_A$ components, the average square of velocity difference between neutrals and ions in the frictional heating Equation 14 can be written by

$$|\mathbf{u}_n - \mathbf{u}_i|^2_{RMS} = |\left(\mathbf{u}_n - \mathbf{u}_i\right)\cdot\hat{\mathbf{z}}|^2 + \frac{\Omega_i^2}{\nu_{in}^2 + \Omega_i^2}\left|\frac{\mathbf{E}_S + \mathbf{u}_n \times \mathbf{B}}{B}\right|^2 + \frac{\Omega_i^2}{\nu_{in}^2 + \Omega_i^2}\left|\frac{\mathbf{E}_A}{B}\right|^2_{\text{RMS}}. \tag{28}$$

The second and third terms on the right-hand side mean the Joule heating by quasistatic electric fields and Alfvén waves, respectively. Note that the momentum equations in Equations 7 and 11 do not include $\mathbf{E}_A$, which drives no net ion and electron motion.

2.4. Numerical Implementation

As defined in Section 2.3, the x, y, and z axes are directed eastward, northward, and upward, respectively. We conduct two-dimensional simulations in which all physical quantities are assumed to be uniform along the x axis (zonal direction). The numerical domain was defined as 0 to 4,000 km on the z axis and −6,000 to 6,000 km on the y axis. Vertical and horizontal resolutions are 5 and 20 km, respectively. The time resolution is 0.03 s. The Alfvénic heating is updated every 1 min. In these settings, we simulate neutral responses for 3 hr.

We separate the numerical domain into "main region" (0–700 km altitude) and "buffer region" (700–4,000 km altitude). In the main region, we solve the neutral, ion, and electron Equations 1–15. In the buffer region, all neutrals and ions are assumed to be at rest, that is, $\mathbf{u}_n = \mathbf{u}_i = 0$. The neutral temperature has no vertical gradient ($\partial T_n/\partial z = 0$), and ion and electron temperature are fixed from the initial values. In addition, the densities in the buffer region are calculated using the diffusion equilibrium rather than the continuity equation as shown below:

$$\begin{cases} \dfrac{\partial n_s}{\partial z} = -\dfrac{n_s}{H_s}(s = \text{neutral}) \\ \dfrac{\partial n_t}{\partial z} = -\dfrac{n_t}{H_{t,\text{eff}}} - \dfrac{n_t}{T_p}\dfrac{\partial T_p}{\partial z}(t = \text{ion}) \end{cases}, \tag{29}$$

where

$$\frac{1}{H_{t,\text{eff}}} = \frac{1}{H_t} - \frac{T_e}{T_i}\frac{1}{H_p}, \tag{30}$$

$$T_p = \frac{T_e + T_i}{2}, H_s = \frac{k_B T_s}{m_s G}, H_p = \frac{2k_B T_p}{m_i G}.$$

$H_{t,\text{eff}}$ means the "effective" scale height for ion species t. For light ions, this can be negative. Using the profiles of neutrals, ions, and electrons in both the main and buffer region, we calculate Alfvén waves by solving Equations 22

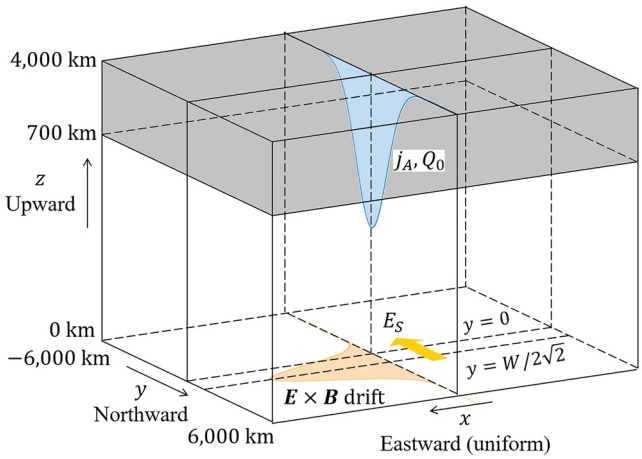

Figure 1. Schematic illustration showing the geometry of the simulation. The x, y, and z axes are directed eastward, northward, and upward, respectively. The region from 700 to 4,000 km altitude is a buffer to calculate Alfvén waves, where all neutrals, ions, and electrons are rest and have fixed temperatures.

and 23 throughout all altitudes (0–4,000 km). The boundary conditions are as follows: At $y = \pm 6,000$ km, $\partial f/\partial y = 0$ for any physical quantity f. At $z = 0$ km, $\mathbf{u}_n = \mathbf{u}_i = 0, \partial T_n/\partial z = \partial T_i/\partial z = \partial T_e/\partial z = 0$, and $\partial n_s/\partial z = 0$ for all neutral and ion species s.

As energy inputs, we impose the precipitating energy flux Q, quasistatic southward electric field E_S, and Alfvénic FAC j_A as follows:

$$\begin{cases} Q(y) = Q_0 \exp\left[-\left(\dfrac{y}{W/2}\right)^2\right] \\ j_A(y) = j_{A0} \exp\left[-\left(\dfrac{y}{W/2}\right)^2\right] \\ E_S(y) = -E_{S0} \exp\left[-\left(\dfrac{y}{W/2} - \dfrac{1}{\sqrt{2}}\right)^2\right] \end{cases}, \tag{31}$$

where W is the horizontal scale size and set to be 200 km (Oigawa et al., 2021). The electron energy flux (Q_0) is 1.6 mW m^{-2} and the characteristic energy is 100 eV as typical values in the cusp (Newell & Meng, 1988). Using the distribution of Alfvénic FAC, we calculate Alfvén heating by summing over all modes (every frequency and wavelength) at each spatial location. Figure 1 is a schematic representation of the simulation's geometry.

The NRLMSISE-00 model (Picone et al., 2002) is used to calculate the initial condition of neutrals, and the IRI-2016 model is used for ions and electrons (Bilitza et al., 2017). We use the following model input parameters $F_{10.7} = 100$ and $A_p = 10$. We also use relevant values from these models in which the date is assumed to be 21:00 UT on 22 December 2018, and the location to be at 70°N and 150°W, as was used in Oigawa et al. (2021). As stated in Section 2.2, we assume that the neutrals, ions, and electrons are all in equilibrium at the start without any external forcing (Oigawa et al., 2021; Shinagawa & Oyama, 2006). The precipitating energy flux Q, quasistatic electric field E_S, and Alfvénic FAC j_A are all imposed as step functions at $t = 0$.

2.5. Modeling Runs

To compare the contributions of quasistatic electric fields and Alfvén waves to the Joule heating and neutral mass density enhancements, we performed five modeling cases. In Case 0, we only impose quasistatic electric fields with $E_S = 60$ mV m^{-1}, which is the same setting as used by Oigawa et al. (2021). Different magnitudes of Alfvén waves are used in Cases 1-1, 1–2, and 1–3 in the absence of quasistatic electric fields. Case 2 includes both energy inputs. The input parameters E_S and j_A in each case are summarized in Table 1 (the resulting mass density changes are also shown).

3. Results

3.1. Example of Alfvén Waves Calculated by the New Method

We refer to heating rates per unit volume as volumetric heating rates expressed by Equations 13–15. On the other hand, heating rates per unit mass are specific heating rates. For example, the specific Joule (neutral-ion frictional) heating rate is Q_{ni}/ρ_n. The specific heating rate plays a significant role in the neutral response by directly affecting the neutral temperature (see Equation 3).

Here, we show an example in which $j_{A0} = 20\,\mu$A m^{-2}. Alfvén waves are reflected between the E region and the sharp slope of the Alfvén velocity much above the F region (at several 1,000 km altitudes), and some are finally absorbed (Belyaev et al., 1999). This process is called the ionospheric Alfvén resonator (IAR). The PSD of electric fields and FACs is shown in Figure 2 to be frequency-wavelength dependent. Standing waves with a fundamental frequency of around 0.9 Hz exist, and they reproduce the structure of IAR.

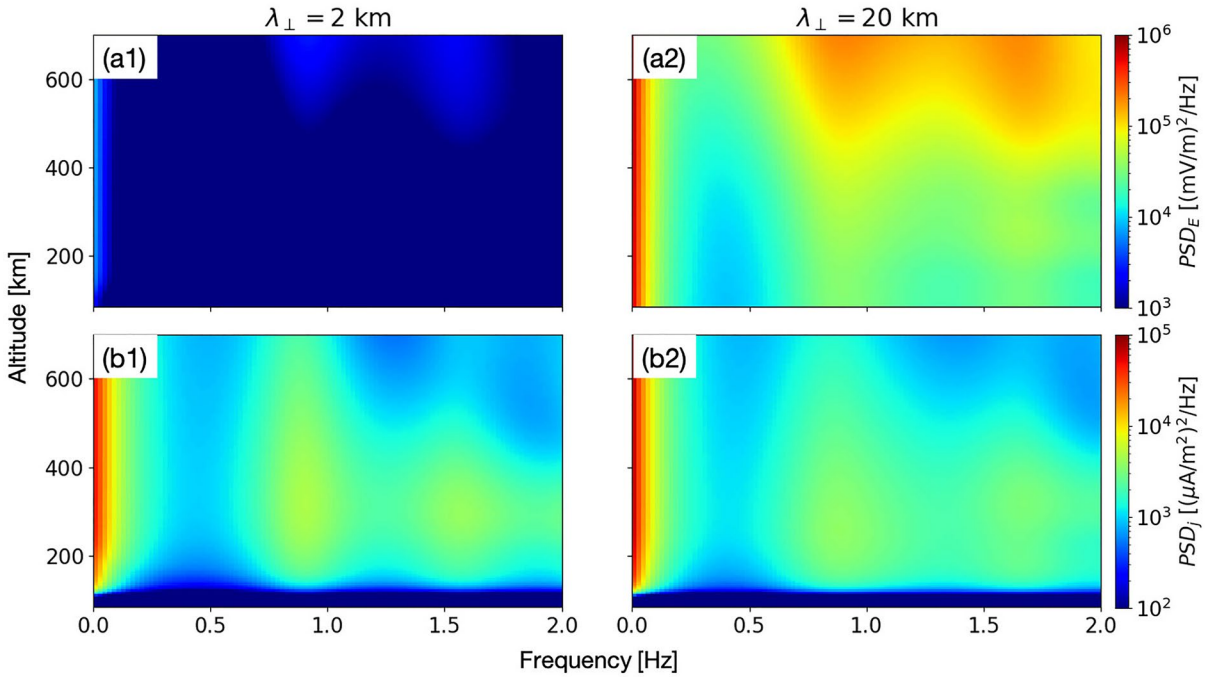

Figure 2. The frequency-wavelength dependency of power spectrum density (PSD) of electric fields (a) and field-aligned currents (FACs) (b). The plots on the left-handed side, that is, a1 and b1 indicate the values for $\lambda_\perp = 2$ km, while the plots on the right-handed side, that is, a2 and b2 are for $\lambda_\perp = 20$km.

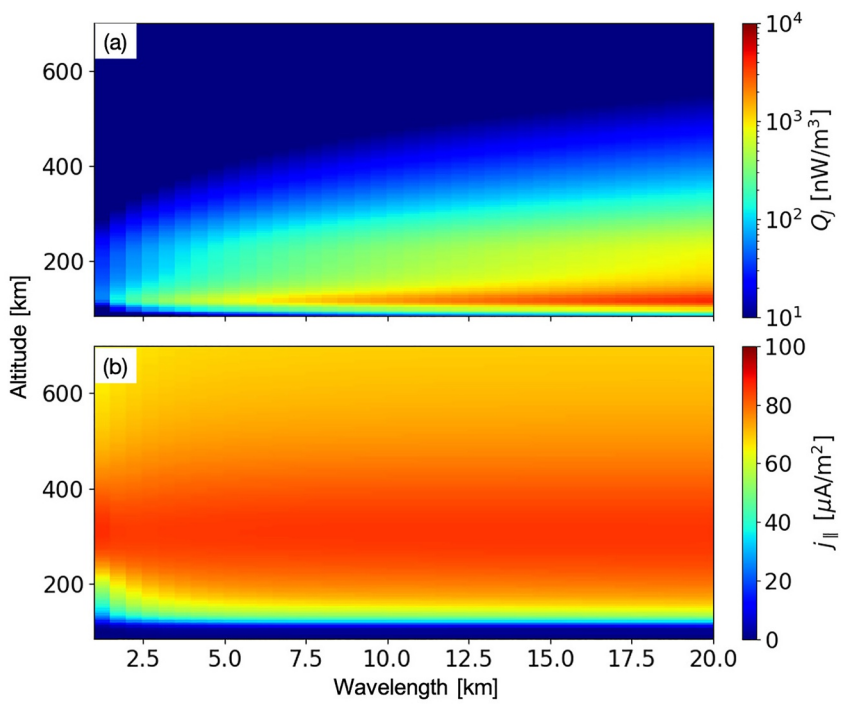

Figure 3. Wavelength-altitude plots of the RMS of Joule heating rate (a) and field-aligned current (FAC) density (b), which are derived by summing up the power spectrum density (PSD) for the whole frequency. The color map in Joule heating (a) is plotted in a log scale.

Table 1
Summary of the Modeling Runs Indicating Two Input Parameters and Output Mass Density Enhancements at 400 km Altitude

	E_{S0} [mV m^{-1}]	j_{A0} [μA m^{-2}]	$\Delta\rho/\rho_0$ at 400 km
Case 0	60	0	9.8%
Case 1-1	0	10	9.3%
Case 1–2	0	15	13.9%
Case 1–3	0	20	32.3%
Case 2	60	20	36.7%

Note. In Case 1, we impose only quasistatic electric fields. In Cases 1-1, 1–2, and 1–3, different magnitudes of Alfvén waves are adopted without quasistatic electric fields. Both energy inputs are included in Case 2.

If the medium were homogeneous in z, the phase difference between Q and J would be $\pi/2$ (a node of one field located at an antinode of the other) for a non-dissipative standing Alfvén wave owing to the z derivative in Equation 23 (Lysak, 1991). The E region and F region (110–400 km altitudes combined) are highly dissipative, while the region below the E region (<110 km) is non-dissipative due to the low ion density. In Figure 2a2, the electric field is non-zero in both dissipative and non-dissipative regions. In contrast, we can see in Figure 2b2 that the FAC vanishes below 110 km, indicating that the phase difference becomes nearly $\pi/2$. This result is consistent with that presented in the Supporting Information S1 of Lotko and Zhang (2018). FACs we have imposed here are constant to wavelength, and electric fields are reverse proportional. As a result, the electric field for wavelength 20 km (Figure 2a2) is stronger than that for wavelength 2 km (Figure 2a1), while the FAC is nearly the same. We have provided additional descriptions of the wavelength dependency of electric fields in Supporting Information S1.

Figure 3 depicts wavelength-altitude plots (at $y = 0$) of the RMS of Joule heating rate and FAC calculated by summing the PSD over the entire frequency range. The prominent feature in Figure 3a is significant Joule heating rates at the F region (150–250 km altitudes) as well as at the E region (110–120 km altitudes). Quasistatic electric fields, almost uniform against height, primarily heat the thermosphere in the E region where the Pedersen conductivity reaches the maximum. In contrast, Alfvén waves cause significant heating rates at the F region because their antinode (or node) is at the F (E) region. These distinguishing features are consistent with Lotko and Zhang's results (2018). It is evident in Figure 3b that FACs with shorter wavelengths do not penetrate deeply due to stronger magnetic diffusion.

3.2. Overview of the Resulting Neutral Mass Density Enhancements

Figures 4a–4c shows meridional-vertical (y-z) plots of neutral mass density change, neutral temperature change, and eastward neutral velocity at 3 hr in each case, respectively. In Figure 4a, the vector field indicates y-z neutral flow velocity. When the heating is weak (Cases 0 and 1-1), mass density increases primarily at altitudes of 450–650 km and only slightly at 400 km. In Case 1–2, however, another mass density cell, whose magnitude is similar to that at altitudes of 450–650 km, is generated at 300–450 km altitude. In Cases 1–3 and 2, this lower-altitude mass density cell is enhanced through more intense heating. The value of the Poynting flux for each case at the center is shown in Figure 4a1–4a5. We can see from Case 1–3 (Figure 4a4) that the Alfvénic Poynting flux of approximately 19 mW m^{-2} creates the fractional density change that is higher than 30%.

When Figure 4b4 (also Figure 4b3 and 4b5) is compared with Figure 4a4 (also Figure 4a3 and 4a5), we notice that the altitude of the maximum temperature change is located at a lower altitude than the peak of the fractional density change. The aforementioned two-peak pattern does not occur in the temperature (Figure 4b) and neutral velocity in the y-z plane (arrows in Figure 4a).

In this two-dimensional simulation, there are no gradients to the east-west direction. As a result, neutral winds in this direction are primarily driven by eastward $\mathbf{E} \times \mathbf{B}$ drift (the Coriolis force is tiny in this direction). Since Alfvén waves do not generate net ion flows, we can only see significant eastward neutral winds in Cases 0 and 2 (Figure 4c1 and 4c5, respectively), where quasistatic electric fields are imposed.

The altitude profiles at the center ($y = 0$) are shown in Figure 5. Figures 5a–5c represents the fractional density change, neutral temperature change, and vertical neutral velocity, respectively. In each figure, the results from five cases are plotted. The vertical neutral velocity (Figure 5c) is the upward component of the neutral velocity shown with arrows in Figure 4a.

It is clear in Figure 5a that the fractional density change in Cases 1–3 and 2 exceeds 30% as shown in Table 1. The peak is located at an altitude between 350 and 400 km as seen in Figure 4a4. Figure 5b shows that the maximum neutral temperature change occurs at lower altitudes as was mentioned above. We find in Figure 5c that there is almost no difference in vertical velocity between Cases 1–3 and 2. This indicates that when the Alfvén waves having $j_{A0} = 20\,\mu$A m^{-2} exist, neutral upwelling is driven by the Alfvén waves, and that the quasistatic electric fields do not contribute to neutral upwelling substantially.

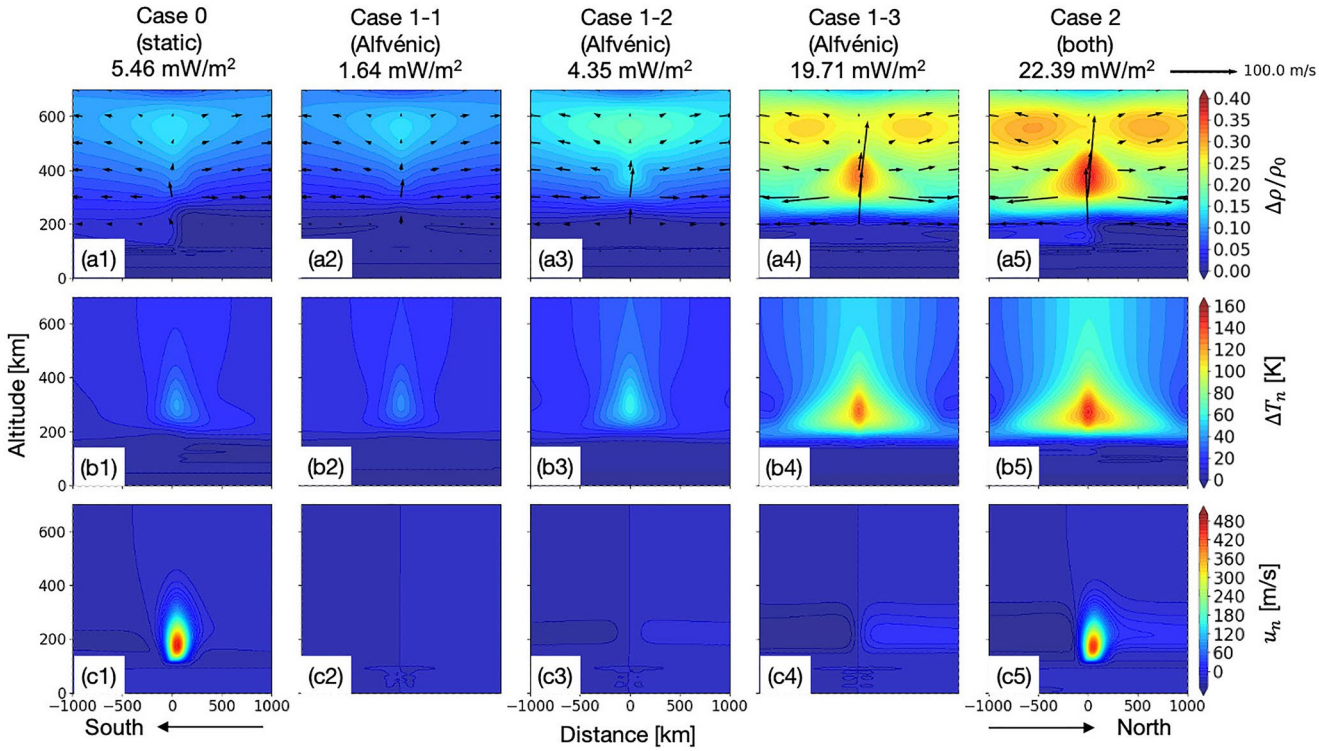

Figure 4. Meridional-vertical (y–z) plots of neutral mass density change (4a1–4a5), neutral temperature change (4b1–4b5), and eastward neutral velocity (4c1–4c5) at 3 hr in each case. The vector field in the top row (4a1–4a5) indicates y-z neutral flow velocity.

3.3. Altitude Profiles of Heating Rates by Quasistatic Electric Fields and Alfvén Waves

Figures 6a and 6b depicts the volumetric heating rates for Cases 0 and 1-1, respectively, which have nearly identical mass density enhancements (see Figure 5). For comparison, the volumetric heating rate caused by the particle precipitation (shown in green) is plotted in both figures. The volumetric heating rates for Case 0 (blue) and Case 1-1 (red) are similar at altitudes of ~300 km but completely different at the E region altitude (110–120 km). The peak value is 150 nW m^{-3} in Case 0 (quasistatic) but only 29 nW m^{-3} in Case 1-1 (Alfvénic), nearly five times smaller. We notice that, under such a great difference in the volumetric heating rate in the E region, similar

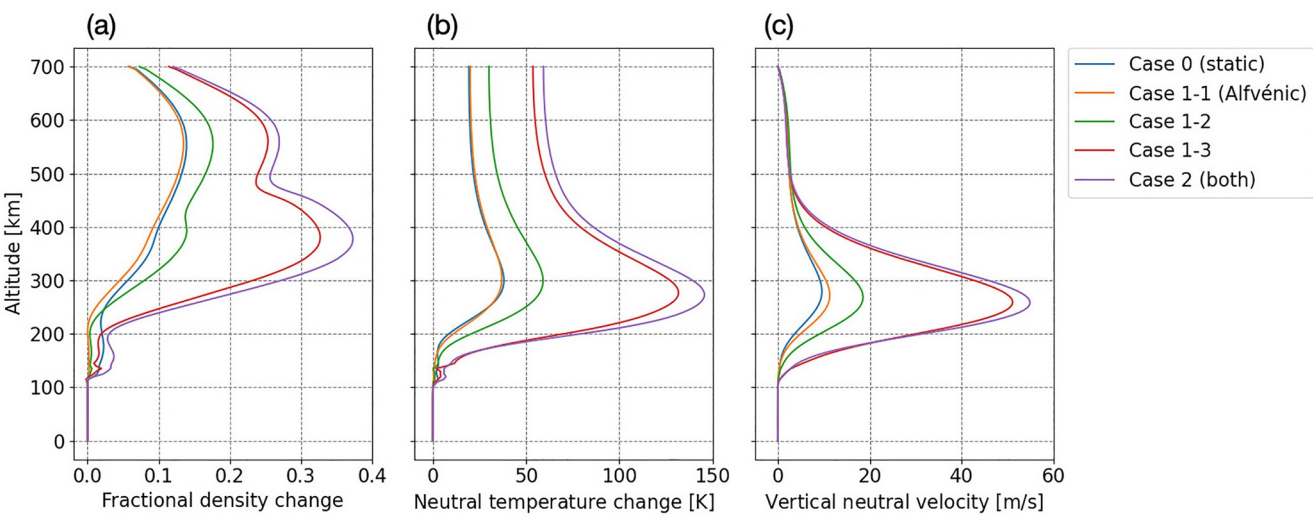

Figure 5. The neutral mass density change (a), neutral temperature change (b), and upward neutral speed (c) at the center (y = 0 km) in each case.

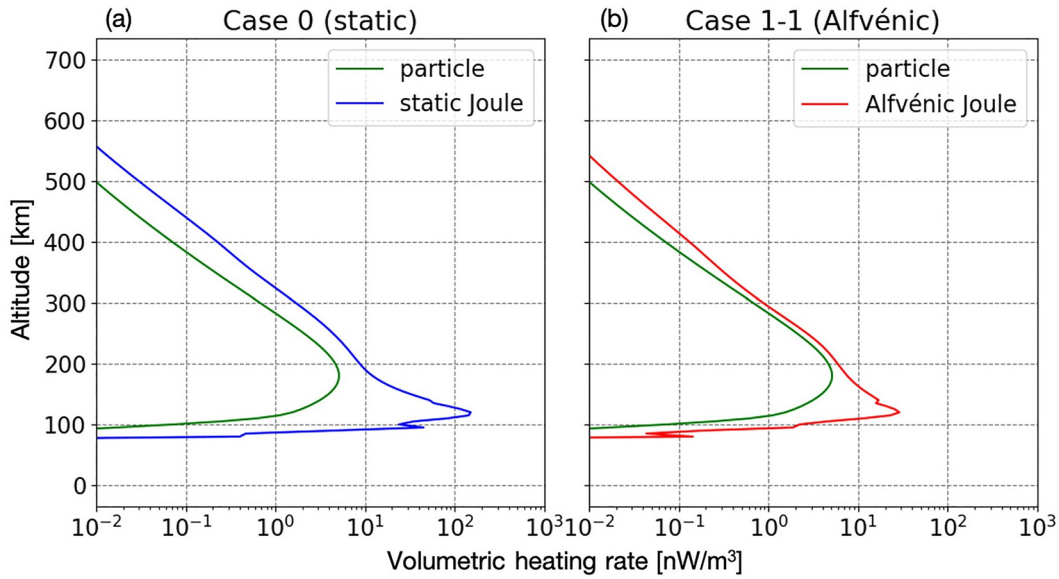

Figure 6. The volumetric heating rates for Cases 0 (a) and 1-1 (b), in which the mass density enhancements in the *F* region (shown in Figure 5a) are almost the same.

altitude profiles of the mass density enhancement in the *F* region are obtained, indicating that heating at the *E* region does not substantially affect the neutral response at the *F* region.

4. Discussion

4.1. Spatial Structure of the Mass Density Enhancement

In Figure 7, we show the time versus altitude plots of the fractional mass density change, upward neutral velocity, and the related three derivatives that constitute dw_n/dt, that is, $\partial w_n/\partial t$, $v_n \partial w_n/\partial y$, and $w_n \partial w_n/\partial z$ for Cases 0 and 2. In both cases, the values at $y = 0$ are shown. Comparison between Figure 7a1 (Case 0) and 7a2 (Case 2) shows that strong oscillatory enhancements are generated above 300 km altitudes by rapidly initiating heating in a step function manner, whereas in Case 0 similar faint oscillatory enhancements can be seen. These enhancements are due to atmospheric gravity waves (Oigawa et al., 2021; their Figure 4a). Those oscillatory enhancements form a stable one at 450–650 km altitudes in 40 min or later in both cases, but its decay is prominent in Case 2.

Figure 7a2 also shows that a mass density enhancement at 300–450 km altitudes, which is shown in Figure 4a3, 4a4, and 4a5, becomes evident after ~60 min. In Figure 7b2, we can see that upward flow stably exists at altitudes below this mass density enhancement. This upward flow also exists in the case of the quasistatic electric field (Case 0) although the velocity is slow. In both cases, the magnitude of $\partial w_n/\partial t$ (shown in Figure 7c1 and 7c2) becomes very small after ~60 min, indicating that the vertical forces are well balanced after ~60 min.

Figure 7d1 and 7d2 shows that $v_n \partial w_n/\partial y$ is very small for both cases during whole 180 min. It is evident from Figure 7e1 and 7e2 that after ~60 min stable flow acceleration and deceleration in the z direction occur at altitudes below and above the stable upward flow, respectively, in Case 2.

That deceleration (shown in reddish color in Figure 7e2) occurs at the altitudes of the lower-altitude mass density enhancement. Considering that the vertical speed w_n is associated with the heating rate, the advection term, $w_n \partial w_n/\partial z$ can be related to the heating rate in a different manner. For example, if the vertical speed w_n is proportional to the heating rate, the advection term can be proportional to the square of the heating rate, meaning that the large advection is crucial for producing intense heating.

To investigate this role, we have performed additional modeling runs for various inputs. We show the results from those 16 runs in Figure 8, where the fractional density change, neutral temperature change, vertical neutral velocity, vertical advection, buoyancy, and vertical viscosity are plotted against the specific heating rate. The parameterization of the 16 runs (including 5 cases in Table 1) is summarized in Table 2. We took the values at

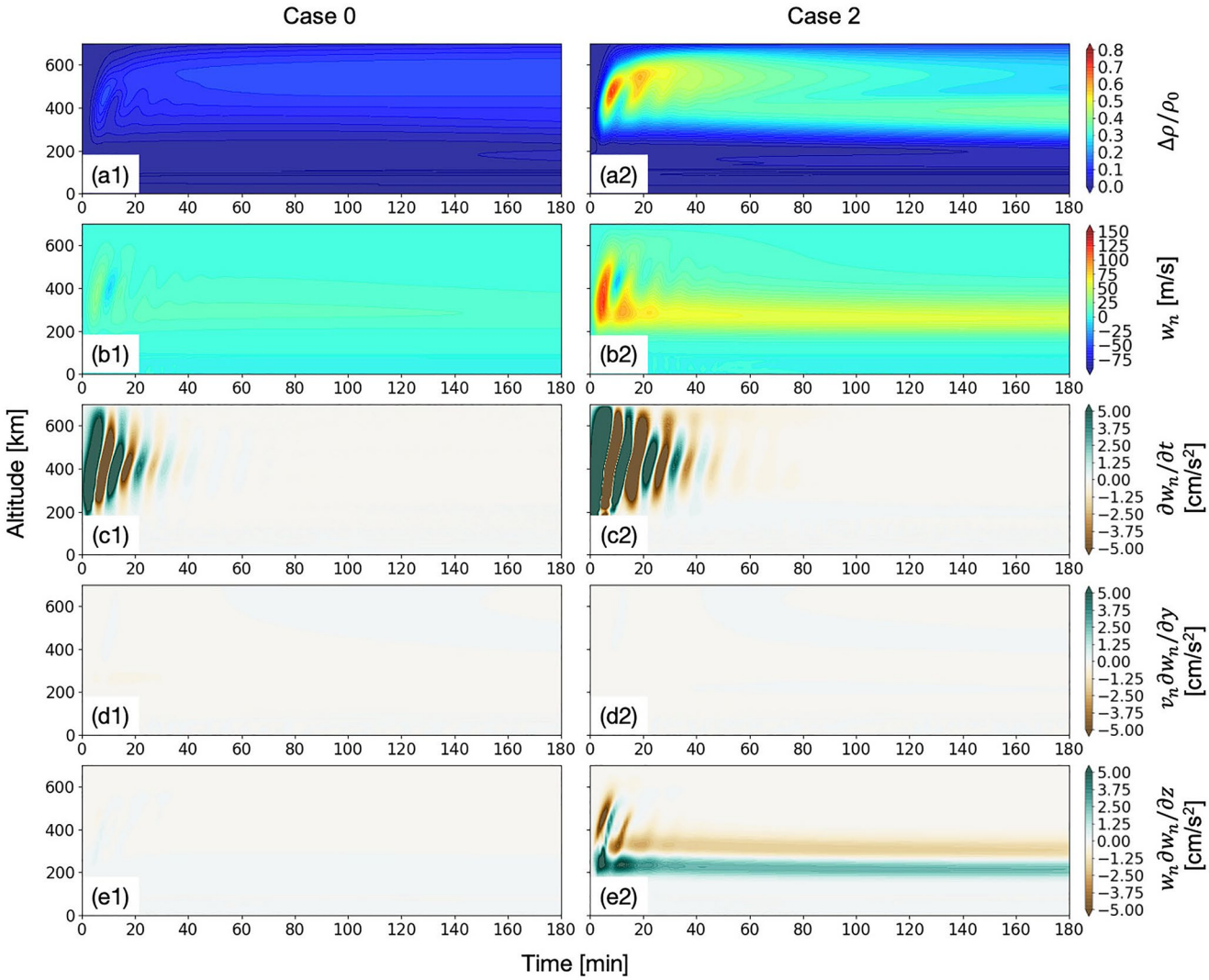

Figure 7. The time evolution of the fractional mass density change, upward neutral velocity, and the related three derivatives that constitute dw_n/dt, that is, $\partial w_n/\partial t$, $v_n\partial w_n/\partial y$, and $w_n\partial w_n/\partial z$ for Cases 0 and 2.

300 km altitude except for the fractional density change. For the fractional density change, we took the value at 400 km altitude because the lower-altitude enhancement occurs around that altitude. In each figure, we have also plotted the regression lines in the log-log scale. The correlation coefficients are very high for all of Figure 8 (over 0.92 for Figures 8a–8d), although the correlation is somewhat lower in Figures 8e and 8f.

The coefficient of $\log_{10}x$ on the right-handed side of the equation for all of Figure 8 except for Figure 8d is less than one (from 0.66 to 0.93). It should be noted that the coefficient of the equation in Figure 8d, that is, the coefficient for vertical advection is 1.44, exceeding 1. This indicates that the advection term at 300 km altitude dominantly affects the mass density enhancements that occur at ~400 km altitude. Lühr et al. (2004) proposed the basic idea that the atmosphere is heated by ionospheric current at a lower level, for example, in the *E* region, where there is then an upwelling of warm air causing a density enhancement at 400 km and above. Our result is consistent with the idea proposed by Lühr et al. (2004) in that the lower altitude region is important for the cusp density enhancement at 400 km altitude. More specifically, however, our result reveals the *F* region altitude of ~300 km is important, rather than the *E* region.

Figures 9a and 9b shows relationships of the fractional density change at two altitudes (400 and 550 km) to the specific heating rate at 300 km altitude and the Alfvénic Poynting flux for Cases 1-1, 1–2, and 1–3. When the specific heating rate at 300 km is relatively small, the fractional density change at 400 km altitude is smaller than

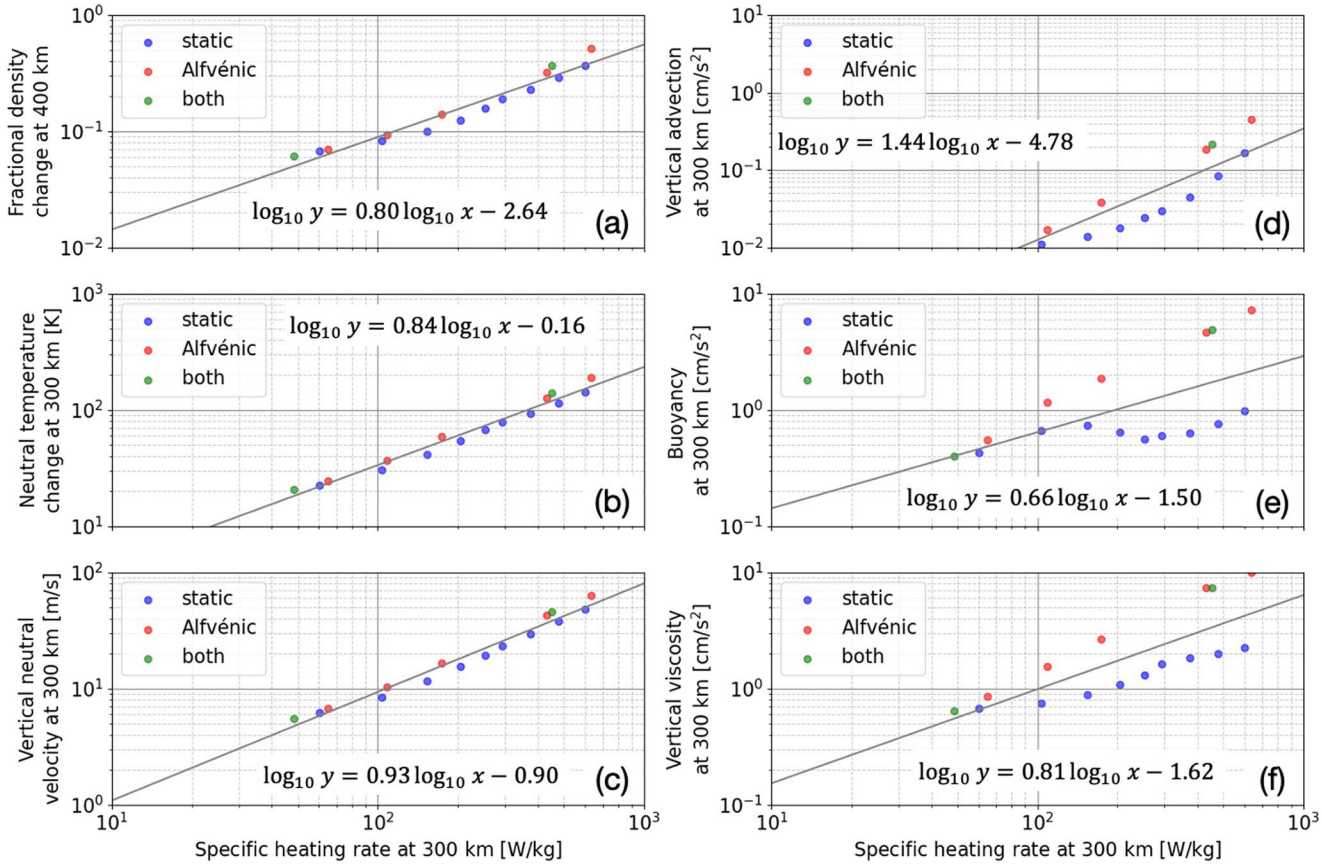

Figure 8. Relation of the fractional density change, neutral temperature change, vertical neutral velocity, vertical advection, buoyancy, and vertical viscosity to the specific heating rate. For the fractional density change, the value at 400 km is used, while the values at 300 km altitude are used for other five parameters. The line in each figure represents the regression line.

that at 550 km altitude. For that specific heating rate, not much deceleration of the upwelling occurs immediately above 300 km altitude, resulting in a modest density increase at an altitude of 400 km. As the specific heating rate increases, the deceleration at an altitude immediately above 300 km becomes greater, thereby effectively increasing the density at altitudes of 350–400 km. Thus, the two lines in Figure 9a crossover. That seems to occur when the specific heating rate at 300 km altitude exceeds roughly 300 W kg^{-1}. In terms of the Alfvénic Poynting flux, the lower-altitude mass density enhancement becomes stronger than the higher-altitude mass density enhancement when the Alfvénic Poynting flux exceeds roughly 11 mW m^{-2}. We can also see in Figure 9 that the specific heating rate of 400 W kg^{-1} at 300 km altitude or the Alfvénic Poynting flux of 20 mW m^{-2} can create the average value of mass density enhancements (~30%). Figure 10 is a schematic illustration representing the above-mentioned scenario for the generation of the mass density enhancements.

4.2. Comparison With Previous Studies

Živković et al. (2015) have analyzed three conjugate observation events by CHAMP and Cluster during geomagnetically quiet conditions in the cusp. The measured mass density enhancements, Poynting flux, and FACs were 20%, 6.50 mW m^{-2}, and 18 μA m^{-2} in the first event, 17%, 12.25 m Wm^{-2}, and 5.48 μA m^{-2} in the second event, and 11%, 9.8 mW m^{-2}, and 8.85 μ Am^{-2} in the last event, respectively. These results are similar to our findings in Cases 1-1 and 1–2 for the mass density change and Poynting flux. It should be noted that for the FAC density, values much higher than the above average values, sometimes exceeding 100 μA m^{-2}, are actually observed. Rother et al. (2007) also show that the maximum of FACs at the cusp can easily exceed 100 μA m^{-2}. These values are consistent with the value at 400 km altitude in our model (Figure 3b).

Table 2
Summary of the Parameterization of the 16 Runs (including Five Cases in Table 1)

	E_{S0} [mV m^{-1}]	j_{A0} [μA m^{-2}]	
Static	20	0	–
–	40	0	–
–	60	0	Same as Case 0
–	80	0	–
–	100	0	–
–	120	0	–
–	140	0	–
–	160	0	–
–	180	0	–
Alfvénic	0	5	–
–	0	10	Same as Case 1-1
–	0	15	Same as Case 1-2
–	0	20	Same as Case 1-3
–	0	25	–
Both	0	0	–
–	60	20	Same as Case 2

Lotko and Zhang (2018) have shown that superposed Alfvén wave electric fields at frequencies from 0.05 to 2 Hz and perpendicular wavelengths from 0.5 to 20 km mainly heat the *F* region. In this regard, our modeling result is consistent with Lotko and Zhang's (2018). The value of the neutral mass density enhancements, however, was not calculated by Lotko and Zhang (2018). In our study, a new method for treating Alfvén resonator modes was developed. We have shown that the Alfvénic Poynting flux of roughly 20 mW m^{-2}, which is consistent with the values from the observation on an average condition, can explain the observation of the neutral mass density enhancements through the neutral upwelling process caused by the Joule heating in ~300 km altitude (Case 1–3 or Case 2).

Hogan et al. (2020) recently investigated the effects of Alfvénic heating on neutral mass density variation, where Alfvén waves were assumed to be constant and uniform in the cusp region over 24 hr. Given that the cusp is highly variable in both time and space, these assumptions are quite simple. The method presented in our study can calculate much more detailed profiles of Alfvénic heating. We have updated the impact of Alfvén waves every minute.

5. Conclusions

We have developed a new efficient method to calculate Alfvén waves. In previous studies, Alfvén waves have been usually calculated by time-domain schemes, such as the FDTD method. The Fourier transform was used in our research, and Alfvén waves were solved as frequency-domain boundary value problems. By solving a system of linear equations once, we could obtain

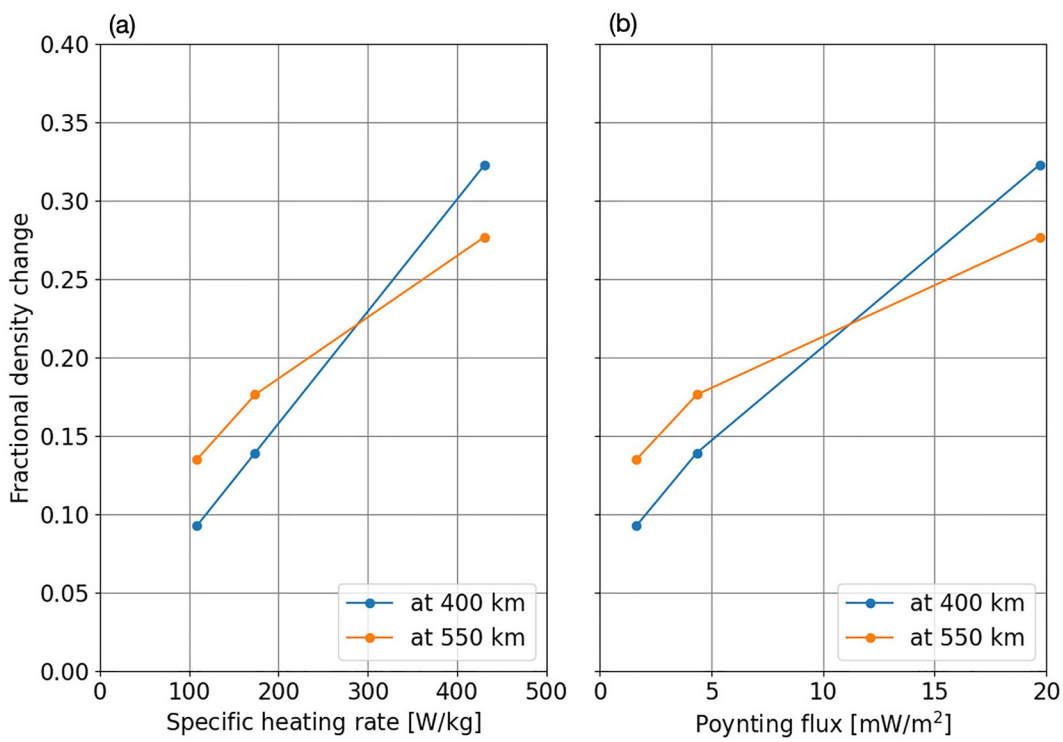

Figure 9. Relationships of the fractional density change at two altitudes (400 and 550 km) to the specific heating rate at 300 km altitude and the Alfvénic Poynting flux for Cases 1-1, 1–2, and 1–3.

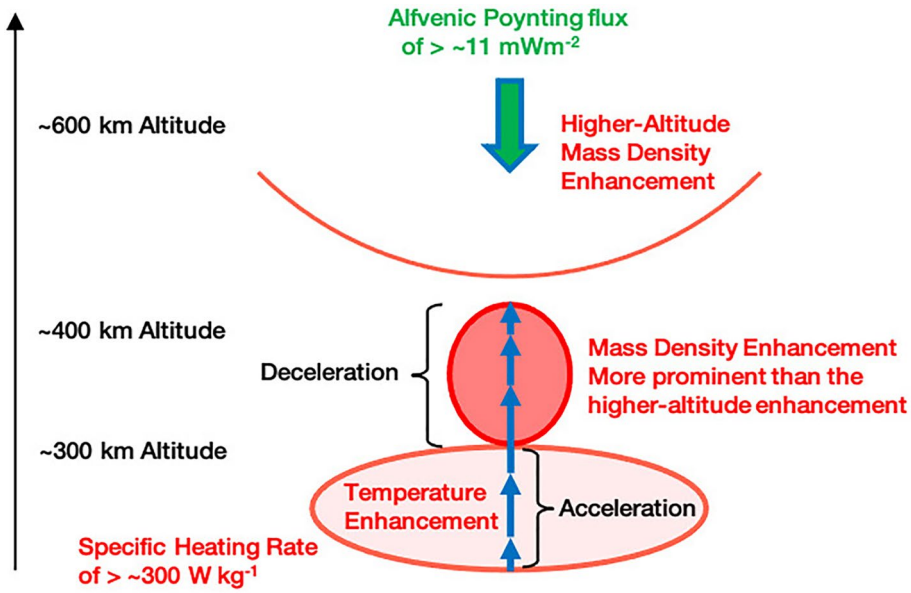

Figure 10. Schematic illustration representing the scenario for the generation of the mass density enhancements.

the altitude profile of electric fields, magnetic fields, and FAC for each frequency and wavelength, and capture temporally and spatially variable features in the cusp. The following conclusions are obtained.

1. A fractional mass density enhancement becomes evident at altitudes centered between 350 and 400 km roughly 1 hr after the Alfvén resonator modes are set up, although a very modest enhancement appears before that time. The cell of the mass density enhancement continues to exist stably for 2 more hours.
2. The Alfvén resonator mode having a field-aligned current of 20 μA m^{-2}, which corresponds to Alfvénic Poynting flux of ∼20 mW m^{-2}, can create a fractional mass density enhancement of slightly more than 30% at 400 km altitude, which is consistent with the result obtained from satellite observations (Kervalishvili & Lühr, 2013; Živković et al., 2015).
3. Comparison between the 300–450 km altitude and 450–650 km altitude mass density enhancements at the time of 3 hours after the Alfvén resonator modes are set up shows that the lower-altitude one becomes stronger than the higher-altitude one when the specific heating rate at 300 km altitude exceeds roughly 300 W kg^{-1}. In terms of the Alfvénic Poynting flux, this corresponds to ∼11 mW m^{-2}.

Appendix A: Chemical Reactions

The right-hand side of the ion continuity Equation 4 denotes local source terms due to ionization, recombination, and other chemical reactions. We employ Fang et al.'s (2010) empirical model to derive the ionization rates caused by electron precipitation. The electron energy flux is 1.6 mW m^{-2}, and the characteristic energy is 100 eV. These values are the same as those used in Oigawa et al. (2021). The bimolecular chemical reactions and recombinations included in the model are written in Tables A1 and A2, accompanying corresponding reaction rates. These values are summarized in Schunk and Nagy (2009).

Table A1
Bimolecular Chemical Reactions and Corresponding Reaction Rates

No.	Reaction	Reaction rate $[m^3 s^{-1}]$
1	$O_2^+ + NO \rightarrow NO^+ + O_2$	4.6×10^{-16}
2	$O_2^+ + N \rightarrow NO^+ + O$	1.5×10^{-16}
3	$N_2^+ + O_2 \rightarrow O_2^+ + N_2$	5.0×10^{-17}
4	$N_2^+ + NO \rightarrow NO^+ + N_2$	4.1×10^{-16}
5	$N_2^+ + O \rightarrow NO^+ + N$	1.3×10^{-16}
6	$N_2^+ + O \rightarrow O^+ + N_2$	9.8×10^{-18}
7	$O^+ + O_2 \rightarrow O_2^+ + O$	2.1×10^{-17}
8	$O^+ + N_2 \rightarrow NO^+ + N$	1.2×10^{-18}
9	$O^+ + NO \rightarrow NO^+ + O$	8.0×10^{-19}
10	$O^+ + H \rightarrow H^+ + O$	6.4×10^{-16}
11	$N^+ + O_2 \rightarrow O_2^+ + N$	3.07×10^{-16}
12	$N^+ + O_2 \rightarrow NO^+ + O$	2.32×10^{-16}
13	$N^+ + O_2 \rightarrow O^+ + NO$	4.6×10^{-17}
14	$He^+ + O_2 \rightarrow O^+ + O + He$	9.7×10^{-16}
15	$He^+ + N_2 \rightarrow N_2^+ + He$	5.2×10^{-16}
16	$He^+ + N_2 \rightarrow N^+ + N + He$	7.8×10^{-16}
17	$H^+ + O \rightarrow O^+ + H$	3.75×10^{-16}

Table A2
Recombination of Ions and Corresponding Recombination Rates

No.	Species	Recombination rate $[m^3 s^{-1}]$
1	O_2^+	$2.4 \times 10^{-13}(300/T_e)^{0.70}$
2	N_2^+	$2.2 \times 10^{-13}(300/T_e)^{0.39}$
3	NO^+	$4.0 \times 10^{-13}(300/T_e)^{0.5}$
4	O^+	$3.7 \times 10^{-18}(250/T_e)^{0.7}$
5	N^+	$3.6 \times 10^{-18}(250/T_e)^{0.7}$
6	He^+	$4.8 \times 10^{-18}(250/T_e)^{0.7}$
7	H^+	$4.8 \times 10^{-18}(250/T_e)^{0.7}$

Data Availability Statement

All simulated data used in this study can be accessed from this site (http://step0ku.kugi.kyoto-u.ac.jp/data/simulation/2021/). Computer resources were provided by Academic Center for Computing and Media Studies, Kyoto University.

Acknowledgments
This work is supported by the Kyoto University Foundation and JSPS KAKENHI Grant 22H01285.

References

Banks, P. M., & Kockarts, G. (1973). *Aeronomy. Part B*. Academic Press.
Belyaev, P. P., Bösinger, T., Isaev, S. V., & Kangas, J. (1999). First evidence at high latitudes for the ionospheric Alfvén resonator. *Journal of Geophysical Research*, *104*(A3), 4305–4317. https://doi.org/10.1029/1998JA900062
Bilitza, D., Altadill, D., Truhlik, V., Shubin, V., Galkin, I., Reinisch, B., & Huang, X. (2017). International Reference Ionosphere 2016: From ionospheric climate to real-time weather predictions. *Space Weather*, *15*(2), 418–429. https://doi.org/10.1002/2016SW001593

Billett, D. D., Perry, G. W., Clausen, L. B. N., Archer, W. E., McWilliams, K. A., Haaland, S., et al. (2021). The relationship between large scale thermospheric density enhancements and the spatial distribution of Poynting flux. *Journal of Geophysical Research: Space Physics*, *126*(5), e2021JA029205. https://doi.org/10.1029/2021JA029205

Brinkman, D. G., Walterscheid, R. L., Clemmons, J. H., & Hecht, J. H. (2016). High-resolution modeling of the cusp density anomaly: Response to particle and Joule heating under typical conditions. *Journal of Geophysical Research: Space Physics*, *121*(3), 2645–2661. https://doi.org/10.1002/2015JA021658

Burleigh, M., & Zettergren, M. (2017). Anisotropic fluid modeling of ionospheric upflow: Effects of low-altitude anisotropy and thermospheric winds. *Journal of Geophysical Research: Space Physics*, *122*(1), 808–827. https://doi.org/10.1002/2016JA023329

Consolini, G., De Michelis, P., Alberti, T., Giannattasio, F., Coco, I., Tozzi, R., & Chang, T. T. S. (2020). On the multifractal features of low-frequency magnetic field fluctuations in the field-aligned current ionospheric polar regions: Swarm observations. *Journal of Geophysical Research: Space Physics*, *125*(5), e2019JA027429. https://doi.org/10.1029/2019JA027429

Crowley, G., Knipp, D. J., Drake, K. A., Lei, J., Sutton, E., & Lühr, H. (2010). Thermospheric density enhancements in the dayside cusp region during strong B_y conditions. *Geophysical Research Letters*, *37*(7), L07110. https://doi.org/10.1029/2009GL042143

Deng, Y., Fuller-Rowell, T. J., Ridley, A. J., Knipp, D., & Lopez, R. E. (2013). Theoretical study: Influence of different energy sources on the cusp neutral density enhancement. *Journal of Geophysical Research: Space Physics*, *118*(5), 2340–2349. https://doi.org/10.1002/jgra.50197

Deng, Y., Maute, A., Richmond, A. D., & Roble, R. G. (2009). Impact of electric field variability on Joule heating and thermospheric temperature and density. *Geophysical Research Letters*, *36*(8), L08105. https://doi.org/10.1029/2008GL036916

Fang, X., Randall, C. E., Lummerzheim, D., Wang, W., Lu, G., Solomon, S. C., & Frahm, R. A. (2010). Parameterization of monoenergetic electron impact ionization. *Geophysical Research Letters*, *37*(22), L22106. https://doi.org/10.1029/2010GL045406

Gary, J. B., Heelis, R. A., & Thayer, J. P. (1995). Summary of field-aligned Poynting flux observations from DE 2. *Geophysical Research Letters*, *22*(14), 1861–1864. https://doi.org/10.1029/95gl00570

Hogan, B., Lotko, W., & Pham, K. (2020). Alfvénic thermospheric upwelling in a global geospace model. *Journal of Geophysical Research: Space Physics*, *125*(12), e2020JA028059. https://doi.org/10.1029/2020JA028059

Kervalishvili, G. N., & Lühr, H. (2013). The relationship of thermospheric density anomaly with electron temperature, small-scale FAC, and ion up-flow in the cusp region, observed by CHAMP and DMSP satellites. *Annales Geophysicae*, *31*(3), 541–554. https://doi.org/10.5194/angeo-31-541-2013

Lotko, W., & Zhang, B. (2018). Alfvénic heating in the cusp ionosphere-thermosphere. *Journal of Geophysical Research: Space Physics*, *123*(12), 10368–10383. https://doi.org/10.1029/2018JA025990

Lühr, H., Park, J., Gjerloev, J. W., Rauberg, J., Michaelis, I., Merayo, J. M. G., & Brauer, P. (2015). Field-aligned currents' scale analysis performed with the Swarm constellation. *Geophysical Research Letters*, *42*, 1–8. https://doi.org/10.1002/2014GL062453

Lühr, H., Rother, M., Köhler, W., Ritter, P., & Grunwaldt, L. (2004). Thermospheric up-welling in the cusp region: Evidence from CHAMP observations. *Geophysical Research Letters*, *31*(6), L06805. https://doi.org/10.1029/2003GL019314

Lysak, R. L. (1991). Feedback instability of the ionospheric resonant cavity. *Journal of Geophysical Research*, *96*(A2), 1553–1568. https://doi.org/10.1029/90JA02154

Lysak, R. L. (1999). Propagation of Alfvén waves through the ionosphere: Dependence on ionospheric parameters. *Journal of Geophysical Research*, *104*(A5), 10017–10030. https://doi.org/10.1029/1999JA900024

Matsuo, T., & Richmond, A. D. (2008). Effects of high-latitude ionospheric electric field variability on global thermospheric Joule heating and mechanical energy transfer rate. *Journal of Geophysical Research*, *113*(A7), 7309. https://doi.org/10.1029/2007JA012993

Matsuo, T., Richmond, A. D., & Hensel, K. (2003). High-latitude ionospheric electric field variability and electric potential derived from DE-2 plasma drift measurements: Dependence on IMF and dipole tilt. *Journal of Geophysical Research*, *108*(A1), 1005. https://doi.org/10.1029/2002JA009429

Maynard, N. C., Heppner, J. P., & Egeland, A. (1982). Intense, variable electric fields at ionospheric altitudes in the high latitude regions as observed by DE-2. *Geophysical Research Letters*, *9*, 981–984. https://doi.org/10.1029/GL009i009p00981

Mur, G. (1981). Absorbing boundary conditions for the finite-difference approximation of the time-domain electromagnetic-field equations. *IEEE Transactions on Electromagnetic Compatibility*, *23*(4), 377–382. https://doi.org/10.1109/TEMC.1981.303970

Newell, P. T., & Meng, C. I. (1988). The cusp and the cleft/boundary layer: Low-altitude identification and the statistical local time variation. *Journal of Geophysical Research*, *93*(A12), 14549–14556. https://doi.org/10.1029/JA093iA12p14549

Oigawa, T., Shinagawa, H., & Taguchi, S. (2021). Time-dependent responses of the neutral mass density to fixed magnetospheric energy inputs into the cusp region in the thermosphere during a period of large IMF B_y: A high-resolution two-dimensional local modeling. *Earth Planets and Space*, *73*(1), 201. https://doi.org/10.1186/s40623-021-01535-9

Picone, J. M., Hedin, A. E., Drob, D. P., & Aikin, A. C. (2002). NRL-MSISE-00 empirical model of the atmosphere: Statistical comparisons and scientific issues. *Journal of Geophysical Research*, *107*(A12), SIA15. https://doi.org/10.1029/2002JA009430

Ridley, A. J., Deng, Y., & Toth, G. (2006). The global ionosphere-thermosphere model. *Journal of Atmospheric and Solar-Terrestrial Physics*, *68*(8), 839–864. https://doi.org/10.1016/j.jastp.2006.01.008

Roble, R. G., & Ridley, E. C. (1994). A thermosphere-ionosphere- mesosphere-electrodynamics general circulation model (TIME-GCM): Equinox solar cycle minimum simulations (30–500 km). *Geophysical Research Letters*, *21*(6), 417–420. https://doi.org/10.1029/93GL03391

Roble, R. G., Ridley, E. C., Richmond, A. D., & Dickinson, R. E. (1988). A coupled thermosphere/ionosphere general circulation model. *Geophysical Research Letters*, *15*(12), 1325–1328. https://doi.org/10.1029/GL015i012p01325

Rother, M., Schlegel, K., & Lühr, H. (2007). CHAMP observation of intense kilometer-scale field-aligned currents, evidence for an ionospheric Alfvén resonator. *Annales Geophysicae*, *25*(7), 1603–1615. https://doi.org/10.5194/angeo-25-1603-2007

Schunk, R., & Nagy, A. (2009). *Ionospheres* (2nd ed.), (Vol. 4). Cambridge University Press.

Schunk, R. W., & Walker, J. C. G. (1970). Transport properties of the ionospheric electron gas. *Planetary and Space Science*, *18*(11), 1535–1550. https://doi.org/10.1016/0032-0633(70)90029-2

Shinagawa, H., & Oyama, S. (2006). A two-dimensional simulation of thermospheric vertical winds in the vicinity of an auroral arc. *Earth Planets and Space*, *58*(9), 1173–1181. https://doi.org/10.1186/BF03352007

Smithtro, C. G., & Solomon, S. C. (2008). An improved parameterization of thermal electron heating by photoelectrons, with application to an X17 flare. *Journal of Geophysical Research*, *113*(A8), A08307. https://doi.org/10.1029/2008JA013077

Taguchi, S., Sugiura, M., Winningham, J. D., & Slavin, J. A. (1993). Characterization of the IMF B_y-dependent field-aligned currents in the cleft region based on DE 2 observations. *Journal of Geophysical Research*, *98*(A2), 1393–1407. https://doi.org/10.1029/92JA01014

Walterscheid, R. L., & Schubert, G. (1990). Nonlinear evolution of an upward propagating gravity wave: Overturning, convection, transience, and turbulence. *Journal of the Atmospheric Sciences*, *47*(1), 101–125. https://doi.org/10.1175/1570-0469(1990)047<0101:NEOAUP>2.0.C0;2

Wilder, F. D., Crowley, G., Anderson, B. J., & Richmond, A. D. (2012). Intense dayside Joule heating during the 5 April 2010 geomagnetic storm recovery phase observed by AMIE and AMPERE. *Journal of Geophysical Research*, *117*(A5), A05207. https://doi.org/10.1029/2011JA017262

Yokoyama, Y., Taguchi, S., & Iyemori, T. (2021). Importance of the northward IMF for the quasistatic mesoscale field-aligned currents embedded in the diminished Region 1/2 current system in the dusk sector. *Journal of Geophysical Research: Space Physics*, *126*(8), e2020JA028774. https://doi.org/10.1029/2020JA028774

Yokoyama, Y., Taguchi, S., Iyemori, T., & Hosokawa, K. (2020). The quasipersistent feature of highly structured field-aligned currents in the duskside auroral oval: Conjugate observation via Swarm satellites and a ground all-sky imager. *Journal of Geophysical Research: Space Physics*, *125*(7), e2019JA027594. https://doi.org/10.1029/2019JA027594

Zettergren, M., & Semeter, J. (2012). Ionospheric plasma transport and loss in auroral downward current regions. *Journal of Geophysical Research*, *117*(A6), A06306. https://doi.org/10.1029/2012JA017637

Zhu, Q., Deng, Y., Richmond, A., & Maute, A. (2018). Small-scale and mesoscale variabilitie in the electric field and particle precipitation and their impacts on Joule heating. *Journal of Geophysical Research: Space Physics*, *123*(11), 9862–9872. https://doi.org/10.1029/2018JA025771

Živković, T., Buchert, S., Ritter, P., Palin, L., & Opgenoorth, H. (2015). Investigation of energy transport and thermospheric upwelling during quiet magnetospheric and ionospheric conditions from the studies of low- and middle-altitude cusp. *Annales Geophysicae*, *33*(6), 623–635. https://doi.org/10.5194/angeo-33-623-2015